A new highly scalable, high-order accurate framework for variable-density flows: Application to non-Boussinesq gravity currents

Paul Bartholomew[a,1,3,*], Sylvain Laizet[a,2,3]

[a] *City and Guilds Building, Imperial College London, South Kensington Campus, London, SW7 2AZ*

Abstract

This paper introduces a new code "QuasIncompact3D" for solving the variable-density Navier-Stokes equations in the low-Mach number limit. It is derived from the Incompact3D framework which is designed for incompressible flows [1]. QuasIncompact3D is based on high-order accurate compact finite-differences [2], an efficient 2D domain decomposition [3] and a spectral Poisson solver. The first half of the paper focuses on introducing the low-Mach number governing equations, the numerical methods and the algorithm employed by QuasIncompact3D to solve them. Two approaches to forming the pressure-Poisson equation are presented: one based on an extrapolation that is efficient but limited to low density ratios and another one using an iterative approach suitable for higher density ratios. The scalability of QuasIncompact3D is demonstrated on several TIER-1/0 supercomputers using both approaches, showing good scaling up to $65k$ cores. Validations for incompressible and variable-density low-Mach number flows us-

[☆] This work was funded under the embedded CSE programme of the ARCHER UK National Supercomputing Service (http://www.archer.ac.uk).

[☆☆] The code presented in this work is available from the repository: https://github.com/xcompact3d/Quasincompact3d

[*] Corresponding author

Email addresses: paul.bartholomew08@imperial.ac.uk (Paul Bartholomew), s.laizet@imperial.ac.uk (Sylvain Laizet)

[1] This paper was written by Paul Bartholomew.

[2] This paper was proof-read by Sylvain Laizet.

[3] Declarations of interest: none

ing the Taylor-Green vortex and a non-isothermal mixing layer, respectively, as test cases are then presented, followed by simulations of non-Boussinesq gravity currents in two- and three-dimensions. To the authors' knowledge this is the first investigation of 3D non-Boussinesq gravity currents by means of Direct Numerical Simulation over a relatively long time evolution. It is found that 2D and 3D simulations of gravity currents show differences in the locations of the fronts, specifically that the fronts travel faster in three dimensions, but that it only becomes apparent after the initial stages. Our results also show that the difference in terms of front location decreases the further the flow is from Boussinesq conditions.

Keywords: Numerical simulation, Finite difference methods, Spectral methods, Buoyancy-driven flows

---

1. Introduction

A gravity, or density, current occurs when gravity acts upon a fluid with horizontal variations in density - creating a pressure field which gives rise to predominantly lateral flow [4]. These density differences may be caused by, for example: temperature or moisture content in atmospheric flows [5]; differences in salinity [6], or suspensions of particles in turbidity currents, avalanches and pyroclastic flows [4]. Clearly the ability to predict such flows is of wide applicability, leading to much interest in their study.

When studying buoyancy driven flows, such as gravity currents, the Boussinesq approximation is frequently used. It assumes that for small density variations, their effect is felt only through the buoyancy term, allowing existing incompressible solvers to be used to simulate these flows as done previously by Härtel et al. [7], Necker et al. [8], Espath et al. [9], Dai [10], Dai and Wu [11], Inghilesi et al. [12], Ottolenghi et al. [13, 14] using Direct and Large Eddy simulations. This assumption is inherently limited in scope to cases for which

density variations are of the order $\Delta\rho \lesssim \mathcal{O}(1\%)$. For larger density variations the variable-density Navier-Stokes equations must be used.

Previous numerical studies of gravity currents in the Boussinesq limit have shown that as the flow develops, discrepancies arise between 2D and 3D simulations [9, 8]. This is in contrast with what has been reported for *non*-Boussinesq lock-exchange flows, namely that 3D effects might be ignored [15]. Bonometti et al. [16] and Rotunno et al. [17] show comparison of their results for 2D non-Boussinesq lock-exchange flows with 3D simulations, reporting that the effect of the 2D simplification on the ability to predict the front speeds is minimal. They do not, however, report on the effect upon other flow statistics such as dissipation rates which, as reported by Espath et al. [9], develop differences between 2D and 3D simulations over longer times in the Boussinesq limit. Whilst Rotunno et al. [17] presented DNS results for non-Boussinesq lock-exchange flows, they appear to be only up to non-dimensional time unit $t = 16$ which, as our results show is in the time-frame when differences become apparent in the 2D and 3D simulations. A numerical investigation of high-Reynolds-number constant-volume non-Boussinesq density currents in deep ambient was performed in Bonometti et al. [18] for 2D cases and comparisons were made between the Navier-Stokes equations and a shallow-water one-layer model. High-resolution simulations of non-Boussinesq downslope gravity currents in the acceleration phase have been performed more recently in Dai and Huang [19] but only in a 2D set-up. To the authors' knowledge, to date, no 3D simulations of non-Boussinesq gravity currents have been performed using high-order methods and studied for relatively long-term evolutions.

In this paper we introduce a new code "QuasIncompact3D" for solving the variable-density Navier-Stokes equations built upon the Incompact3D framework [1, 3]. The initial focus is to solving flows subject to the Low Mach

Number (LMN) approximation [20], however as demonstrated in this paper the solver is applicable more generally to variable density flows and is used to study the evolution of a gravity current in 3D lock-exchange set-up beyond the Boussinesq limit over relatively long periods. The Incompact3D framework is based on high-order compact finite-differences [2] for approximation of spatial derivatives and a spectral solver for the direct solution of the Poisson equation. It is combined with a domain decomposition strategy enabling efficient, scalable simulations with billions of mesh nodes using up to $\mathcal{O}\left(10^5\right)$ computational cores [3]. The newly implemented solver is benchmarked for the incompressible Taylor-Green vortex [21, 22] and the non-isothermal mixing layer of Golanski et al. [23]. Its scaling is tested on the TIER-1/0 supercomputers `ARCHER`, `HAZEL HEN` and `MARCONI`. Following these tests, validation for both Boussinesq and non-Boussinesq gravity currents is presented and finally, fully resolved, high-order studies of 3D non-Boussinesq gravity currents.

The paper is laid out as follows: the governing equations and numerical method used in this study are summarised in §2, followed by a validation of the implementation and a scalability study in §3; the study of gravity currents is presented in §4 with further validation of the code for 2D non-Boussinesq lock exchange flows and gravity currents in the Boussinesq limit; conclusions are drawn in §5.

2. Governing equations and numerical method

When variations in fluid density become appreciable ($\mathcal{O}\left(1\%\right)$ or more), driving variations in the flow field through dilatational effects from thermal expansion, mass diffusivity *etc.*, the Boussinesq approximation is no longer valid and the variable-density Navier-Stokes equations must be considered. However, this condition states nothing about the flow speed which may still be low such that

$\gamma M^2 \ll 1$, where γ is the ratio of specific heats and $M = u/a$ is the Mach number with u and a defined as the local flow velocity and speed of sound, respectively. Under these LMN conditions, the equations for compressible flows become ill-conditioned and their numerical solution inefficient due to restrictive timestep requirements. This inefficiency can be seen as arising from the need to resolve processes occurring on acoustic timescales which, due to the significant difference in speed of sound and flow speed, might be considered as essentially instantaneous. The LMN approximation, obtained by taking the asymptotic limit of the compressible flow equations as $M \to 0$ [20] yields a set of equations without the ill-conditioning due to $\gamma M^2 \ll 1$. Derivation of the LMN governing equations proceeds by expanding variables in terms of $\varepsilon = \gamma M^2$, for example the variable ϕ is expanded as:

$$\phi = \phi^{(0)} + \varepsilon\phi^{(1)} + \varepsilon^2\phi^{(2)} + \dots \ . \tag{1}$$

Substituting the expanded variables into the governing equations and taking the lowest order terms in ε yields the LMN governing equations. These are presented below in non-dimensional form with superscripts (0), (1), $\dots$ dropped where the variable is unambiguous (for a detailed derivation see, for example, McMurtry et al. [20])

$$\frac{D\rho}{Dt} = -\rho\boldsymbol{\nabla}\cdot\boldsymbol{u} \ , \tag{2}$$

$$\mathbf{0} = -\boldsymbol{\nabla}p^{(0)} \ , \tag{3}$$

$$\begin{aligned}\frac{\partial\rho\boldsymbol{u}}{\partial t} + \frac{1}{2}\left(\boldsymbol{\nabla}\cdot\rho\boldsymbol{u}\boldsymbol{u} + \rho\boldsymbol{u}\cdot\boldsymbol{\nabla}\boldsymbol{u} + \boldsymbol{u}\left(\rho\boldsymbol{\nabla}\cdot\boldsymbol{u} + \boldsymbol{u}\cdot\boldsymbol{\nabla}\boldsymbol{u}\right)\right) = \\ = -\boldsymbol{\nabla}p^{(1)} + \frac{1}{Re}\boldsymbol{\nabla}\cdot\boldsymbol{\tau} + \frac{1}{Fr^2}\rho\boldsymbol{g} \ ,\end{aligned} \tag{4}$$

$$\rho\frac{DT}{Dt} = \frac{1}{RePr}\boldsymbol{\nabla}^2 T \ , \tag{5}$$

where $D(\cdot)/Dt$ is the material derivative, $\boldsymbol{g}$ is the unit gravity vector, t is time, T is temperature, $\boldsymbol{u}$ the velocity vector, ρ is density and $\boldsymbol{\tau}$ the viscous stress tensor given as

$$\boldsymbol{\tau} = \mu\left(\boldsymbol{\nabla}\boldsymbol{u} + \boldsymbol{\nabla}^T\boldsymbol{u}\right) - \frac{2}{3}\mu\left(\boldsymbol{\nabla}\cdot\boldsymbol{u}\right)\boldsymbol{I}\ . \tag{6}$$

Note that whilst in Eq.(4), the divergence of the viscous stress term is written in conservative form, it is in fact implemented non-conservatively as

$$\begin{aligned}\boldsymbol{\nabla}\cdot\boldsymbol{\tau} =& \mu\left[\boldsymbol{\nabla}^2\boldsymbol{u} + \boldsymbol{\nabla}\cdot\left(\boldsymbol{\nabla}^T\boldsymbol{u}\right) - \frac{2}{3}\boldsymbol{\nabla}\left(\boldsymbol{\nabla}\cdot\boldsymbol{u}\right)\right] \\ &+ \left(\boldsymbol{\nabla}\mu\right)\cdot\left[\boldsymbol{\nabla}\boldsymbol{u} + \boldsymbol{\nabla}^T\boldsymbol{u} - \frac{2}{3}\left(\boldsymbol{\nabla}\cdot\boldsymbol{u}\right)\boldsymbol{I}\right]\ ,\end{aligned} \tag{7}$$

which is done to prevent oscillations in the velocity field if μ is varying in space [24]. In non-dimensionalising the governing equations the Prandtl, Reynolds and Froude numbers naturally arise, given as $Pr = {c_p}^*\mu^*/k^*$, $Re = \rho^*\mathcal{U}^*\mathcal{L}^*/\mu^*$ and $Fr = \mathcal{U}^*/\sqrt{g^*\mathcal{L}^*}$, respectively, with c_p defined as the specific heat capacity at constant pressure, k the thermal conductivity, $\mathcal{U}$ and $\mathcal{L}$ the velocity and length scales used in non-dimensionalising the equations from which the reference time scale $t^* = \mathcal{L}^*/\mathcal{U}^*$ follows. Here, and throughout the rest of this work, the nomenclature of "*bare*" symbols are used to indicate dimensionless variables whilst superscript $*$ represents a dimensional value.

Perhaps the major stand-out of the LMN governing equations is the split of the pressure field into two fields: $p^{(0)}$ and $p^{(1)}$. To see how this occurs, consider the non-dimensional momentum equations for compressible flows

$$\rho\frac{D\boldsymbol{u}}{Dt} = -\frac{1}{\gamma M^2}\boldsymbol{\nabla}p + \frac{1}{Re}\boldsymbol{\nabla}\cdot\boldsymbol{\tau}\ , \tag{8}$$

which highlights the issues experienced when solving the compressible flow equations as $\gamma M^2 \to 0$ with Eq.(8) tending to $\boldsymbol{0} = -\boldsymbol{\nabla}p$ and the governing system

of equations becomes ill-conditioned. Expressing the non-dimensional pressure using the ideal gas law $p = \rho T$ and expanding the density and temperature in terms of ε following Eq.(1), we obtain

$$p = \rho^{(0)}T^{(0)} + \varepsilon\left(\rho^{(0)}T^{(1)} + \rho^{(1)}T^{(0)}\right) + \varepsilon^2\rho^{(1)}T^{(1)} + \dots \ , \tag{9}$$

in which we identify the zeroth and first order terms as the thermodynamic ($p^{(0)}$) and mechanical/dynamic ($p^{(1)}$) pressures, respectively. Substituting this expansion into the momentum equations and expanding all other variables, the lowest order expansion yields the condition that thermodynamic pressure is constant in space Eq.(3) whilst the first order expansion yields the LMN momentum equations Eq.(4) driven by the mechanical pressure, for further details see [25, 23, 20].

2.1. Solution algorithm

QuasIncompact3D uses a variation of the fractional step method introduced by Chorin [26] to integrate the governing equations in time, similar applications of this approach to the LMN equations can be found in Golanski et al. [23], McMurtry et al. [20], Motheau and Abraham [24], Nicoud [27, 28]. The algorithm will be presented in semi-discrete form, with the variables discretised in time where the superscript n represents a variable evaluated at time $t^n = t^0 + n\Delta t$ and casting all transport equations in the form:

$$\left.\frac{\partial \phi}{\partial t}\right|_n^{n+1} = f_\phi^n \ , \tag{10}$$

to express the transient from state n to $n+1$ and f_ϕ^n is the "forcing term" collecting advection, diffusion and source terms evaluated at t^n.

The algorithm proceeds by, with the exception of the momentum equations, integrating all transport equations to time $n+1$, noting that only one of density

or temperature need be advanced in time, the other being obtainable via the equation of state:

$$p^{(0)} = \rho T \ . \tag{11}$$

Following Golanski et al. [23], the density is advanced in time in the present study. Instead of the full timestep, the momentum transient is split into two steps (hence the name fractional step):

$$\left.\frac{\partial \rho \boldsymbol{u}}{\partial t}\right|_{n}^{n+1} = \left.\frac{\partial \rho \boldsymbol{u}}{\partial t}\right|_{n}^{\star} + \left.\frac{\partial \rho \boldsymbol{u}}{\partial t}\right|_{\star}^{n+1} \ , \tag{12}$$

$$\left.\frac{\partial \rho \boldsymbol{u}}{\partial t}\right|_{n}^{\star} = \boldsymbol{f}_u^n \ , \tag{13}$$

$$\left.\frac{\partial \rho \boldsymbol{u}}{\partial t}\right|_{\star}^{n+1} = -\boldsymbol{\nabla} {p^{(1)}}^{n+1} \ , \tag{14}$$

where the first term accounts for only advection, viscous stress and body force terms to obtain an intermediate state $\star$ and the second transient completes the timestep by "correcting" the velocity field with the new pressure field.

The obvious approach to construct an equation for pressure is to take the divergence of Eq.(14) resulting in a pressure-Poisson equation of the form:

$$\boldsymbol{\nabla}^2 {p^{(1)}}^{n+1} = \frac{1}{\Delta t}\left(\boldsymbol{\nabla}\cdot(\rho\boldsymbol{u})^{\star} - \boldsymbol{\nabla}\cdot(\rho\boldsymbol{u})^{n+1}\right) \ . \tag{15}$$

This approach is attractive as it results in a constant-coefficient Poisson equation, suitable for fast Poisson solvers, however the term $\boldsymbol{\nabla}\cdot(\rho\boldsymbol{u})^{n+1}$ requires knowing the velocity field at time t^{n+1} and must be estimated. Using backward finite-differences in time, $\boldsymbol{\nabla}\cdot(\rho\boldsymbol{u})^{n+1}$ is approximated as Golanski et al. [23]:

$$\boldsymbol{\nabla}\cdot(\rho\boldsymbol{u})^{n+1} = -\left.\frac{\partial \rho}{\partial t}\right|^{n+1} \approx -\frac{\rho^{n+1}-\rho^n}{\Delta t} \ , \tag{16}$$

where the backward finite-difference scheme must be chosen consistently with the rest of the discretisation [23, 28]. Whilst the ability to use fast Poisson solvers makes this an efficient approach, Nicoud [28] showed that it does not enforce the velocity divergence criterion given by Eq.(17). However it is found to be applicable for density ratios in the range $\mathcal{O}(3) - \mathcal{O}(5)$. Whilst the divergence of momentum at time t^{n+1} is unknown, the divergence of velocity can be obtained with a combination of Eq.(2), Eq.(3) and Eq.(5), giving

$$\widehat{\boldsymbol{\nabla} \cdot \boldsymbol{u}}^{n+1} = \frac{1}{p^{(0)} RePr} \boldsymbol{\nabla}^2 T^{n+1} \ , \tag{17}$$

where T^{n+1} is already known via ρ^{n+1} and the equation of state. The hat notation is introduced to differentiate the divergence of velocity constraint from the divergence of the velocity field. By dividing Eq.(14) by ρ^{n+1} in advance of taking the divergence, the following variable-coefficient Poisson equation for pressure is obtained

$$\boldsymbol{\nabla} \cdot \frac{1}{\rho^{n+1}} \boldsymbol{\nabla} {p^{(1)}}^{n+1} = \frac{1}{\Delta t} \left(\boldsymbol{\nabla} \cdot \boldsymbol{u}^{\star} - \boldsymbol{\nabla} \cdot \boldsymbol{u}^{n+1} \right) \ , \tag{18}$$

which enforces the velocity divergence constraint exactly. To use a fast Poisson solver, Eq.(18) is rearranged as a constant-coefficient Poisson equation with a correction term

$$\begin{aligned} \boldsymbol{\nabla}^2 {p^{(1)}}^{\nu+1} = \boldsymbol{\nabla}^2 {p^{(1)}}^{\nu} + \widetilde{\rho} \Bigg[\frac{1}{\Delta t} \left(\boldsymbol{\nabla} \cdot \boldsymbol{u}^{\star} - \widehat{\boldsymbol{\nabla} \cdot \boldsymbol{u}}^{n+1} \right) \\ - \boldsymbol{\nabla} \cdot \frac{1}{\rho^{n+1}} \boldsymbol{\nabla} {p^{(1)}}^{\nu} \Bigg] \ , \end{aligned} \tag{19}$$

which is solved iteratively in an inner loop as shown in algorithm 1 which summarises the method described above. In Eq.(19) the superscript ν is an iteration counter and $\widetilde{\rho}$ is a density scale, typically taken as the global minimum of density [24], indicated here by $\widetilde{\rho} = \rho^0$, or an average in homogeneous direc-

tions [27, 28]. This choice (in particular $\widetilde{\rho} = \rho^0$) is based on stability of the algorithm [24], however examination of Eq.(19) shows that the value of $\widetilde{\rho}$ does not affect the converged solution and we are thus theoretically free to take any value for this quantity. As the Incompact3D framework is based on a partial staggering of the variables (see §2.2 for details), Eq.(19) is evaluated at the pressure nodes, therefore $\widetilde{\rho}$ must be evaluated also at the pressure nodes. The constant values for $\widetilde{\rho}$ discussed above are by definition valid at all nodes of the mesh, an alternative strategy investigated here is to interpolate the density to the pressure nodes using harmonic averages, indicated here by $\widetilde{\rho} = \rho^h$. The harmonic average has the behaviour of tending to the local value of ρ when density is locally uniform and the minimum value in the stencil when density is varying, as a result the algorithm should be stabilised in variable density areas similarly to the use of $\widetilde{\rho} = \rho^0$ and better scaled where density is approximately constant which should lead to better convergence.

2.2. Numerical methods

For clarity, the governing equations have been presented in semi-discrete form with first-order forward Euler approximation of the transient terms. The implementation in fact uses either multi-step Adams-Bashforth or multi-stage Runge-Kutta methods for time integration so that the density term would be written as:

$$\left.\frac{\partial \rho}{\partial t}\right|^n = \sum_{m=1}^{n} \alpha^m f_\rho^m \tag{20}$$

where superscript m represents either time step or stage as appropriate and α^m are coefficients for the chosen scheme, all other transient terms in algorithm 1 are treated accordingly.

The approximation of spatial derivatives is achieved by compact finite-differences [2], giving for the first- and second-order derivatives the following expressions

while $t^n < t^{end}$ **do**
  Integrate Eq.(10) to obtain ρ^{n+1};
  Integrate Eq.(13) to obtain $(\rho\boldsymbol{u})^\star$;
  Compute $\widehat{\boldsymbol{\nabla}\cdot\boldsymbol{u}}^{n+1}$ using Eq.(17);
  if *Constant-coefficient Poisson equation* **then**
    Approximate $\boldsymbol{\nabla}\cdot(\rho\boldsymbol{u})^{n+1}$ using Eq.(16);
    Solve Eq.(15) for ${p^{(1)}}^{n+1}$;
  else
    while $\left|\left|{p^{(1)}}^{\nu} - {p^{(1)}}^{\nu-1}\right|\right| > tol$ **do**
      Solve Eq.(19) for $p^{\nu+1}$;
    end
    Set ${p^{(1)}}^{n+1} = {p^{(1)}}^{\nu}$;
  end
  Correct velocity $\boldsymbol{u}^{n+1} = \boldsymbol{u}^\star - \dfrac{\Delta t}{\rho^{n+1}}\boldsymbol{\nabla}{p^{(1)}}^{n+1}$;
  Set $n+ = 1$;
end

Algorithm 1: QuasIncompact3D algorithm for solving the LMN governing equations. Starred variables indicate intermediate states arising as part of the fractional-step method [26] with the intermediate velocity and momentum related as $\boldsymbol{u}^\star = (\rho\boldsymbol{u})^\star/\rho^{n+1}$. The superscript n represents a variable evaluated at time $t^0 + n\Delta t$. The parameter *tol* and superscript ν are the absolute tolerance and iteration counter for the inner loop of the variable-coefficient Poisson solver, respectively.

$$\alpha\left.\frac{\partial\phi}{\partial x}\right|_{i-1} + \left.\frac{\partial\phi}{\partial x}\right|_{i} + \alpha\left.\frac{\partial\phi}{\partial x}\right|_{i+1} = a\frac{\phi_{i+1}-\phi_{i-1}}{2\Delta x} + b\frac{\phi_{i+2}-\phi_{i-2}}{4\Delta x} \tag{21}$$

and

$$\alpha\left.\frac{\partial^2\phi}{\partial x^2}\right|_{i-1} + \left.\frac{\partial^2\phi}{\partial x^2}\right|_{i} + \alpha\left.\frac{\partial^2\phi}{\partial x^2}\right|_{i+1} = a\frac{\phi_{i+1}-2\phi_i+\phi_{i-1}}{\Delta x^2} + b\frac{\phi_{i+2}-2\phi_i+\phi_{i-2}}{4\Delta x^2} + c\frac{\phi_{i+3}-2\phi_i+\phi_{i-3}}{9\Delta x^2} \tag{22}$$

respectively with similar expressions for the y and z coordinate axes.

By choosing $\alpha = 1/3,\ a = 14/9$ and $b = 1/9$, Eq.(21) is sixth-order accurate while having a so-called "quasi-spectral behaviour" [2] due to its capabilities to represent accurately a wide range of scales. The compromise of the sixth-order accuracy has been chosen to maintain a compact formulation (a three- and five-node stencil for $\partial\phi/\partial x\big|_i$ and $\partial^2\phi/\partial x^2\big|_i$, respectively) via the use of a Hermitian structure of the scheme with $\alpha \neq 0$. Note however that the present approach can be straightforwardly adapted to centred finite-difference schemes of higher order if necessary.

Similarly, by choosing $\alpha = 2/11,\ a = 12/11,\ b = 3/11$ and $c = 0$, Eq.(22) is sixth-order accurate with the same favourable properties of the first derivative in terms of "spectral-like" resolution [2]. To control the aliasing errors via the viscous term, this type of schemes can be modified by adjusting their spectral property near the mesh cutoff, through the use of a less compact formulation, with for instance $\alpha = 0.47959871686180711,\ a = 0.42090288706093404,\ b = 1.7020738409366740$ and $c = 0.16377929427399390$ that preserves the sixth-order accuracy of the scheme.

To prevent pressure-velocity decoupling the pressure mesh is staggered by half a mesh with respect to the velocity mesh, as described in detail in Laizet and Lamballais [1]. First derivatives and interpolations for this midpoint staggered arrangement are performed using the following expressions

$$\alpha f'_{i-1/2} + f'_{i+1/2} + \alpha f'_{i+3/2} = a\ \frac{f_{i+1} - f_i}{\Delta x} + b\ \frac{f_{i+2} - f_{i-1}}{3\Delta x} \tag{23}$$

with $\alpha = 9/62$, $a = 63/62$ and $b = 17/62$ and

$$\alpha f^I_{i-1/2} + f^I_{i+1/2} + \alpha f^I_{i+3/2} = a\ \frac{f_{i+1} + f_i}{2} + b\ \frac{f_{i+2} + f_{i-1}}{2} \tag{24}$$

with $\alpha = 3/10$, $a = 3/4$ and $b = 1/20$.

The pressure-Poisson equation is solved in spectral space using the modified wave number k' associated with the scheme (23), defined as

$$k'_x \Delta x = \frac{2a \sin\left(k_x \Delta x/2\right) + 2b/3 \sin\left(3k_x \Delta x/2\right)}{1 + 2\alpha \cos\left(k_x \Delta x\right)} \ , \tag{25}$$

where k_x is the actual wavenumber, and the the transfer function associated with the midpoint interpolation scheme (24), expressed as

$$T_x(k_x \Delta x) = \frac{2a \cos(k_x \Delta x/2) + (2b/3) \cos(3k_x \Delta x/2)}{1 + 2\alpha \cos(k_x \Delta x)} \tag{26}$$

The use of modified wave numbers and transfer functions lead to the spectral equivalence with the sixth-order accurate compact finite-difference approximations [1]. For additional details about the numerical methods used in this work, including extension of the spectral solver to non-periodic and non-symmetric boundary conditions, the interested reader is directed to Laizet and Lamballais [1].

2.3. Scalability

The high level of parallelisation in QuasIncompact3D is achieved thanks to a highly scalable 2D domain decomposition library and a distributed Fast Fourier Transform (FFT) interface [3]. This open-source library is available at `http://www.2decomp.org/`. The 3D computational domain is divided into pencils with three different orientations referred to as X-pencil, Y-pencil and Z-pencil (*fig.* 1 from left to right). The derivatives and interpolations in the x-direction (y-direction, z-direction) are performed in X-pencil (Y-pencil, Z-pencil), respectively. The 3D FFTs required by the Poisson solver are also broken down as series of one-dimensional FFTs computed in one direction at a time. The global transpositions to switch from one pencil decomposition to another are performed with the MPI command `MPI_ALLTOALL(V)`.

The scalability of QuasIncompact3D is tested on the TIER-1/0 supercomputers `ARCHER` [29], `MARCONI` [30] and `HAZEL HEN` [31] supercomputers for both the constant- and variable-coefficient Poisson equation approaches. For the interested reader, the system architectures follow: `ARCHER` and `HAZEL HEN` are Cray XC30 and XC40 systems based on 2×12 core Intel® Xeon® processors running at 2.7 GHz and 2.5 GHz respectively using the Aries interconnect (dragonfly topology [32]) and are thus expected to show similar performance; `MARCONI` meanwhile is based on the Intel® Xeon® Phi architecture with 1×68 cores per node running at 1.4 GHz using an Intel® Omnipath® interconnect in a fat tree 2:1 topology.

The problem considered is triply periodic, similar to the Taylor-Green vortex presented in §3.1. For the purposes of these scaling tests, the number of iterations in the variable-coefficient Poisson solver is fixed at 5 per timestep, this choice is a balance between typically observed number of iterations to achieve a very high level of accuracy and computational time. As seen in table 2, the average number of iterations, which is of course problem dependent, could be of order 10. To cover the full range of core counts available to users on `MARCONI` whilst keeping the number of mesh nodes n per core in the approximate range $50k < n/CPU < 1M$, the strong scaling tests were split into two sets: one covering 1 to 16 nodes and one covering 16 to 93 nodes; representing $64 \leq NCPU \leq 1024$ and $1024 \leq NCPU \leq 5952$. A similar approach is taken on `HAZEL HEN` with scaling tests performed on $2048 \leq NCPU \leq 32768$ and $4096 \leq NCPU \leq 65536$ cores for $2048 \times 1024 \times 1024$ and 2048^3 mesh nodes respectively. The scaling tests on `ARCHER` are performed on $1008 \leq NCPU \leq 16128$ cores. Timing data for the strong scaling tests are plotted in *fig.* 1.

The strong scaling results demonstrate that QuasIncompact3D is scalable up to $\mathcal{O}\left(10^4\right)$ cores and maintains scalability across architectures, future bench-

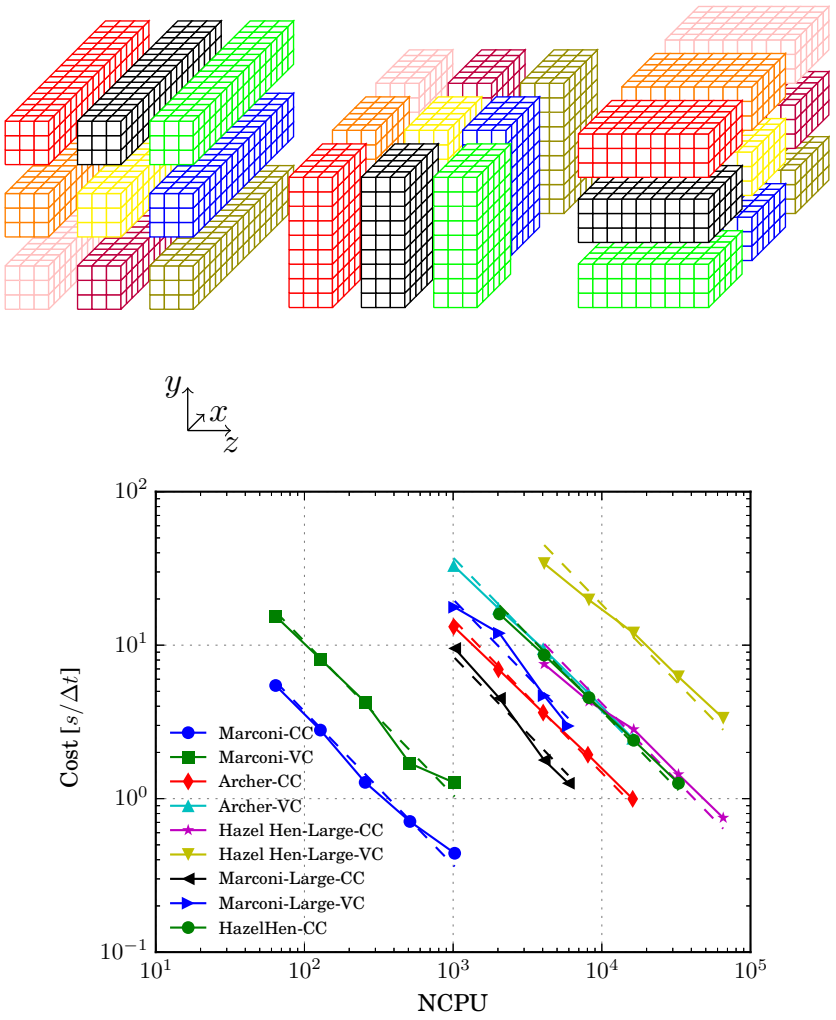

Figure 1: Schematic of the 2D domain decomposition used for parallelisation (top) where colours represent a pencil allocated to one computational core (1 MPI process) in X-, Y- and Z-pencils from left to right. The bottom subfigure shows the strong scaling results for QuasIncompact3D where solid lines with symbols indicate recorded data whilst dashed lines indicate the mean ideal scaling behaviour.

marks on more cores should be as good as Incompact3D. Comparison of the scaling results for the constant- and variable-coefficient Poisson solvers shows that similar scalability is obtained by both, the use of the variable-coefficient Poisson solver simply adds to the per-timestep cost due to the additional cost

of the iterative method.

3. Code validation

To validate the implementation of the code two cases are considered: the 3D Taylor-Green vortex and the 2D non-isothermal mixing layer studied by Golanski et al. [23] to test the LMN solver itself.

3.1. Three-dimensional Taylor-Green vortex

The Taylor-Green vortex is a classical test case for fluid dynamics codes. Given an initial velocity field [21, 22]

$$\boldsymbol{u}\left(x,y,z\right) = \begin{pmatrix} U\sin\left(x\right)\cos\left(y\right)\cos\left(z\right) \\ -U\cos\left(x\right)\sin\left(y\right)\cos\left(z\right) \\ 0 \end{pmatrix} \tag{27}$$

in the periodic box $-\pi \leq x, y, z \leq \pi$, the flow is evolved in time for $0 \leq t \leq 20$ and the volume integrals of kinetic energy and enstrophy computed. For an overview of the flow features the interested reader is directed to Brachet et al. [33]. As an incompressible flow the density is set as uniformly 1 throughout the domain. No initial perturbation is added to the flow. The non-dimensionalisation is based on the velocity U and the domain size.

The evolution of kinetic energy and enstrophy in the domain are plotted in *fig.* 2a and *fig.* 2b respectively. The flow was simulated at $Re = 1,600$, $Pr = 1$[4] using both Incompact3D and QuasIncompact3D using the constant- and variable-coefficient Poisson solvers on a 128^3 mesh and compared with the data of Jammy et al. [21] and Dairay et al. [34] obtained with a 512^3 mesh.

[4] As an incompressible flow, the Prandtl number has no bearing on the results, this test is to confirm the correct behaviour of QuasIncompact3D in the incompressible regime.

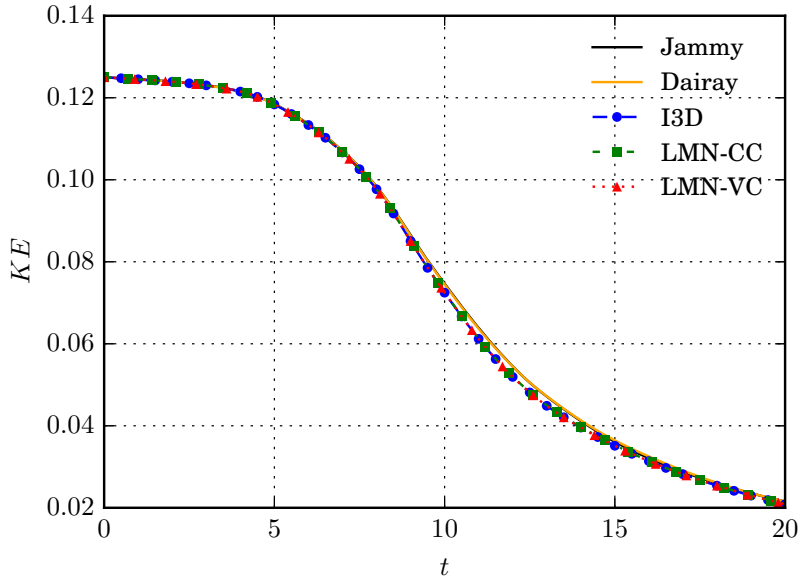

(a) Kinetic energy evolution

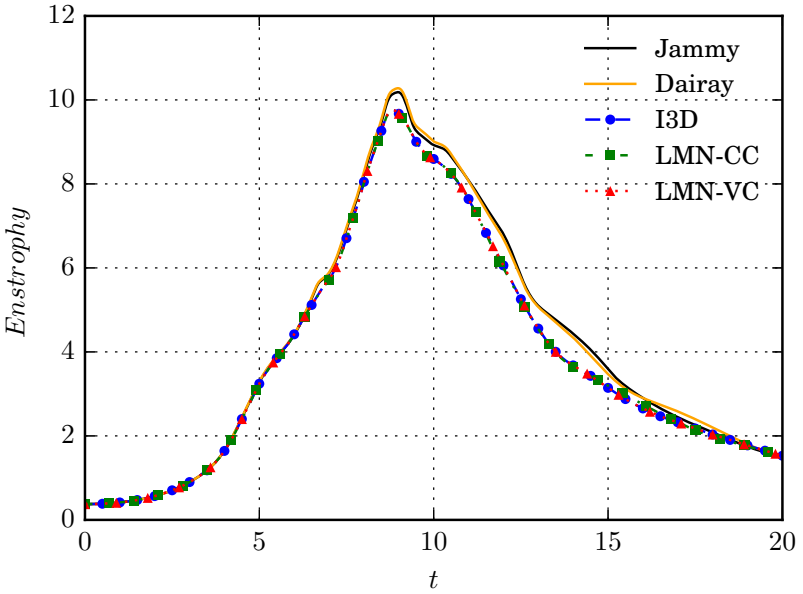

(b) Enstrophy evolution

Figure 2: Time evolution of integrals of kinetic energy and enstrophy for the 3D Taylor-Green vortex. The keys `I3D`, `LMN-CC` and `LMN-VC` correspond to: Incompact3D and QuasIncompact3D using the constant- and variable-coefficient Poisson formulations respectively whilst the reference data of Jammy et al. [21] and Dairay et al. [34] are plotted with continuous lines.

Despite a lower resolution, the present results show good agreement with the reference data of Jammy et al. [21] and Dairay et al. [34]. Most importantly, the results obtained using Incompact3D and QuasIncompact3D are indistinguishable for both the constant- and variable-coefficient Poisson solvers. As the case is incompressible, Incompact3D and QuasIncompact3D should produce the same results, the underlying code being essentially the same for constant densities.

3.2. Two-dimensional non-isothermal mixing layer

The implementation of QuasIncompact3D is validated for variable-density flow against the 2D, non-isothermal mixing layer of Golanski et al. [23]. The flow initially consists of two streams (a "*hot*" and "*cold*" stream, denoted streams 1 and 2) with x velocities u_1 and u_2 and temperatures T_1 and T_2 respectively.

The initial velocity profile is given by the hyper-tangent velocity profile

$$u = \frac{u_1 + u_2}{2} + \frac{u_1 - u_2}{2} \tanh 2y \ , \tag{28}$$

where y is the vertical direction, streams 1 and 2 being above and below the centreline ($y = 0$) respectively. The velocities of the hot and cold streams are constrained by the condition

$$u_c = \frac{\sqrt{T_1}u_2 + \sqrt{T_2}u_1}{\sqrt{T_1} + \sqrt{T_2}} = 0 \ . \tag{29}$$

To promote the transition to mixing [35, 23] the initial velocity field is perturbed by

$$\begin{aligned} u' &= Ae^{-\sigma y^2} \frac{\sigma}{\pi} L_x y \left(\sin\left(8\pi \frac{x}{L_x}\right) + \frac{1}{8}\sin\left(4\pi \frac{x}{L_x}\right) + \frac{1}{16}\sin\left(2\pi \frac{x}{L_x}\right)\right) \ , \\ v' &= Ae^{-\sigma y^2} \left(\cos\left(8\pi \frac{x}{L_x}\right) + \frac{1}{8}\cos\left(4\pi \frac{x}{L_x}\right) + \frac{1}{16}\cos\left(2\pi \frac{x}{L_x}\right)\right) \ , \end{aligned} \tag{30}$$

where δ is the initial mixing layer thickness and A and σ are parameters controlling the strength of the perturbation and its rate of decay from the centreline.

The parameters describing the case are given in table 1 in addition to the domain dimensions L, boundary conditions BC and number of mesh nodes n in each direction. For non-dimensionalisation the velocity difference ${u_1}^* - {u_2}^*$, the density and temperature of the cold stream (stream 2) are used with all other fluid properties assumed constant and δ^* is taken as the length scale.

Table 1: Setup for 2D non-isothermal mixing layer.

Quantity	**Value**	**Quantity**	**Value**
L_x	30.7	L_y	60.0
BC_x	Periodic	BC_y	Free slip
n_x	256	n_y	501
T_1	2	T_2	1
Re	400	Pr	0.75
A	$0.025\,(u_1 - u_2)$	σ	0.05

The flow is simulated until non-dimensional time $t = 200$ using both the constant- and variable-coefficient Poisson solvers, and contours of density compared with those presented by [23] in *fig.* 3.

As *fig.* 3 shows, a good agreement is found between all three variants of the Poisson equation implemented in QuasIncompact3D and the solutions of Golanski et al. [23]. Similar agreement can be found for the comparison of contours of vorticity in the $x-y$ plane, indicating that the underlying implementation of the LMN approximation and different Poisson solvers is working as expected.

An analysis of the performance of the algorithms is presented in table 2 showing the time spent solving the Poisson equation in terms of wall clock time (normalised with respect to the constant-coefficient solver), average number of iterations per (sub) timestep to achieve a very high level of accuracy (for the variable-coefficient solvers, defined as $10^{-11} - 10^{-12}$ in the present study) and the proportion of the simulation time spent in the Poisson solver. As can clearly

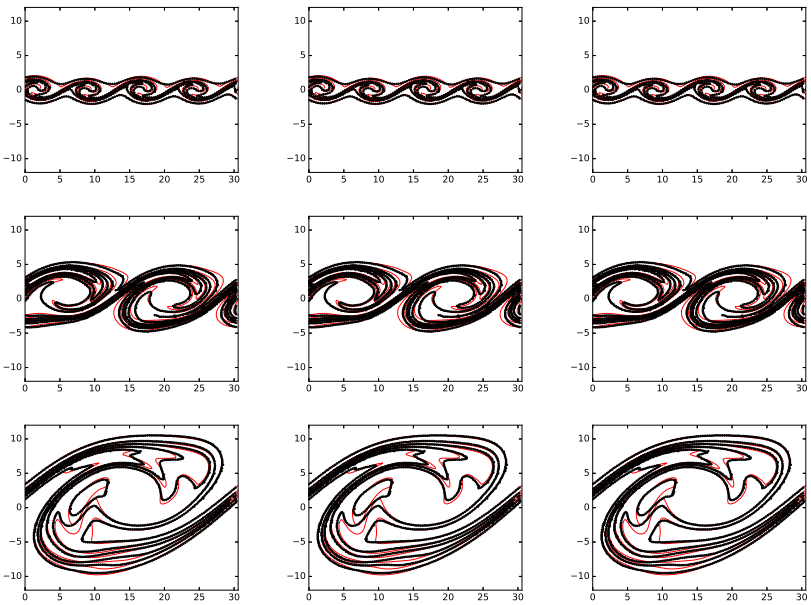

Figure 3: Comparison of density contours obtained with QuasIncompact3D (in black) and those of Golanski et al. [23] (in red) at times $t = 24, 82, 182$ from top to bottom and from left to right using the constant-coefficient Poisson equation, variable-coefficient Poisson equation with $\widetilde{\rho} = \rho^0$ and $\widetilde{\rho} = \rho^h$ respectively and the results of Golanski et al. [23].

be seen in table 2, the constant-coefficient solver is significantly faster than the variable-coefficient solver due to the fixed amount of computational effort per timestep whilst the iteration approach in the variable-coefficient solvers leads to an increase in computational effort as shown in the increased wall clock time and the time spent in the Poisson equation. However, this increased cost is offset by the fact that the corrected velocity field satisfies the divergence criterion up to a very high level of accuracy (up to 5-6 orders of magnitude more accurate than the accuracy for the constant-coefficient solver). Note that for the data presented in table 2, the constant-coefficient solver has an error of the order of 10^{-6} while the error is of the order $10^{-11} - 10^{-12}$ for the variable-coefficient solver. Whilst in the case considered here it does not show any significant effect in the results, this error in the velocity field could potentially place a limit

Table 2: Comparison of algorithm performance showing: wall clock time, normalised by constant-coefficient wall clock time; average number of iterations to converge the Poisson equation at each step; and the cost of the Poisson equation in terms of total runtime. The different solvers are indicated by `CC` and `VC` to represent constant- and variable-coefficient Poisson solvers respectively where the choice of $\widetilde{\rho}$ and stopping criterion are given in brackets.

Algorithm	**Wall Clock**	**Avg. Iterations**	**Poisson Cost** [%]
CC	1	1	18.5
VC (ρ^0, CC err)	4.19	11.7	80.52
VC (ρ^h, CC err)	2.76	6.57	69.48
VC (ρ^0)	12.49	38.2	93.28
VC (ρ^h)	7.04	20.5	88.13

on the applicability of the constant-coefficient solver. It can also be noted that around 10 iterations would be needed for the variable-coefficient solver to match the error of the constant-coefficient solver. Finally, it is important to point out that the good scalability of the variable-coefficient solver is not impacted by the number of iterations.

4. Gravity current study

The code is further validated for 2D gravity currents both in and beyond the Boussinesq limit. For these flows, following Birman et al. [36] and Espath et al. [9, 37], incompressibility is enforced and the density field is determined by a concentration as

$$\rho\left(x\right) = \left(\rho_2 - \rho_1\right) c\left(x\right) + \rho_1 \ , \tag{31}$$

where $0 \leq c \leq 1$ is the concentration and $\rho_1 \geq \rho_2$ are the (constant) fluid densities. As density is a function of concentration the continuity equation becomes

$$\frac{D\rho}{Dt} = \frac{1}{ReSc}\boldsymbol{\nabla}^2\rho \ , \tag{32}$$

where $Sc = \mu/\rho/D$ is the Schmidt number, set at a fixed value $Sc = 1$ for the present simulations, reflecting the value used in the reference data of Birman et al. [36] and Espath et al. [9, 37]. This necessitates modification of the extrapolation step of the constant-coefficient Poisson solver as

$$\boldsymbol{\nabla} \cdot (\rho \boldsymbol{u})^{n+1} = \boldsymbol{u}^{n+1} \cdot \boldsymbol{\nabla} \rho^{n+1} = - \left. \frac{\partial \rho}{\partial t} \right|^{n+1} + \frac{1}{ReSc} \boldsymbol{\nabla}^2 \rho^{n+1} \ , \tag{33}$$

to account for the changed continuity equation; the variable-coefficient Poisson solver is unchanged, requiring only $\widehat{\boldsymbol{\nabla} \cdot \boldsymbol{u}}^{n+1} = 0$ as input. It should be noted that this assumption is only used here in order to make comparisons with the reference data of Birman et al. [36] and Espath et al. [9, 37].

In all the cases that follow, the variables are non-dimensionalised using a combination of the heavy fluid density ρ_1, the buoyancy velocity defined as

$$u_b = \sqrt{g' H} \ , \tag{34}$$

where $g' = (\rho_1 - \rho_2) |\boldsymbol{g}|$ is the reduced gravity, and a length scale H. The kinematic viscosity ν is constant, yielding a constant Reynolds number within each fluid.

Initially the fluid is quiescent and the initial density field is specified as

$$\rho(x) = \frac{1}{2} \left(\frac{\rho_2}{\rho_1} + 1 \right) - \frac{1}{2} \left(1 - \frac{\rho_2}{\rho_1} \right) \operatorname{erf} \left(x' \sqrt{ReSc} \right) \ , \tag{35}$$

where

$$x' = x - x_f^0 \ , \tag{36}$$

and x_f^0 is a problem-dependent parameter defining the initial location of the density discontinuity.

4.1. Validation with 2D gravity currents

The lock-exchange flows with density ratios in the range $0.4 \leq \rho_2/\rho_1 \leq 0.998$, previously studied by Birman et al. [36], are used to validate the solver for both Boussinesq and non-Boussinesq flows at $Re = 4000$. The domain is the rectangle given by $0 \leq x \leq 32H$, $-H/2 \leq y \leq H/2$ meshed with 4097×257 mesh nodes and at each boundary a free-slip condition is applied.

Figure 4 shows snapshots of the density field at $t = 10$ and as it can be seen, an asymmetry develops in the flow the further the density ratio is from Boussinesq conditions. The location of the left travelling light front is nearly independent of density ratio whilst the right travelling dense front shows significantly greater penetration with increasing density ratio - the same behaviour was found by Birman et al. [36]. The subplot of *fig.* 4 corresponding to density ratio $\rho_2/\rho_1 = 0.7$ shows generally good qualitative agreement with *fig.* 3b of Birman et al. [36] (included for comparison). The small differences can be attributed to the use of different flow solvers with different accuracy for the numerical methods.

For quantitative comparison with the results of Birman et al. [36], the following flow statistics are computed:

- The front locations, using the criterion of the dense/light front being the maximum/minimum x of the $c = 0.9$ contour;
- The heavy and light front velocities, computed as:

$$u = \frac{x_f^{k+1} - x_f^k}{t^{k+1} - t^k} \tag{37}$$

  where x_f^{k+1} and x_f^k are the front locations at times t^{k+1} and t^k respectively;
- Energy budgets, specifically the available potential energy, kinetic energy, turbulent dissipated energy and energy dissipated due to mass diffusion,

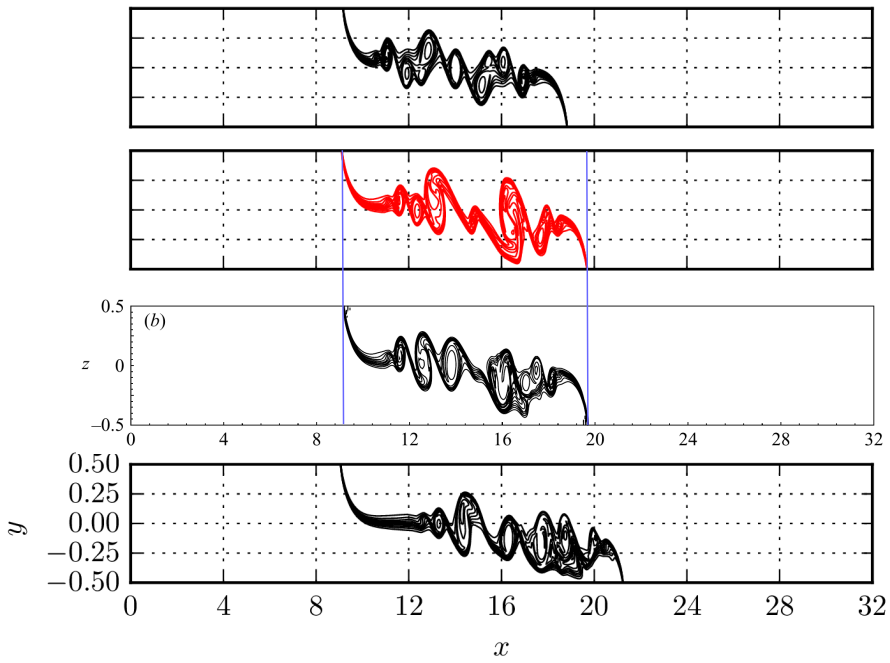

Figure 4: Density contours of 2D lock-exchange at $t = 10$ for density ratios: $\rho_2/\rho_1 = 0.998, 0.7, 0.4$ from top-to-bottom. The middle two figures show $\rho_2/\rho_1 = 0.7$ with the present results above in red and those of Birman et al. [36] *fig.* 3b in black with blue vertical lines to indicate the front locations.

defined as:

$$E_p = -\frac{1}{Fr^2}\int_\Omega (\rho - \rho_2)\, \boldsymbol{g}\cdot\boldsymbol{h} dV \ , \tag{38}$$

$$K = \frac{1}{2}\int_\Omega \rho \boldsymbol{u}^2 dV \ , \tag{39}$$

$$E_d\,(t) = \int_0^t \varepsilon\,(\tau)\, d\tau,\ \varepsilon = \frac{2}{Re}\int_\Omega \rho |\boldsymbol{S}|^2 dV \ , \tag{40}$$

$$E_{\boldsymbol{\nabla}^2\rho}\,(t) = \int_0^t \varepsilon_s\,(\tau)\, d\tau,\ \varepsilon_s = -\frac{1}{Fr^2 ReSc}\int_\Omega (\boldsymbol{g}\cdot\boldsymbol{h})\, \boldsymbol{\nabla}^2\rho dV \ , \tag{41}$$

$$E_{tot} = E_p + K + E_d + E_{\boldsymbol{\nabla}^2\rho} \tag{42}$$

where Ω is the domain, $\boldsymbol{h} \geq \boldsymbol{0}$ the height vector, ε and ε_s the rates of

turbulent dissipation and mass diffusion dissipation respectively and $\boldsymbol{S}$ is the strain rate tensor. For derivations of the above quantities, see Birman et al. [36] and Espath et al. [9]. Note that the energy budgets are evaluated using the same sixth-order finite-difference schemes from the simulations.

Comparisons of front velocities and energy budgets are presented in *fig.* 5 and *fig.* 6, with the reference data of Birman et al. [36] in black and present data in red.

As *fig.* 5 shows, there is a good agreement in the evolution of front velocity between the present work and the reference data of Birman et al. [36], as expected from the qualitative agreement of instantaneous front locations. The only noticeable difference is reported for the density ratio of 0.4, for $t > 10$, and only for the heavy front. A slow reduction of the heavy front velocity can be observed in the reference data of Birman et al. [36], whereas this velocity is almost constant in the present data, in line with the trend observed for the other density ratio. The origin of this difference is not clear but it could be related to the accuracy of the numerical methods (the mesh resolution is very similar). It was noted that the location of the light front was nearly independent of density ratio and this is confirmed in *fig.* 5 with the light front velocity converging to $u_r \simeq 0.5$ for all density ratios. The dense front velocity however shows a strong dependence on the density ratio as observed in the instantaneous density contours.

The comparison of energy budgets also show a good agreement with the reference data. In particular, it is important to notice that the total energy is conserved for the present simulations. One key difference is that the present results account for dissipation of energy by mass-diffusion (Eq.(41)) which was discarded by Birman et al. [36]. The results show that its effect is small, how-

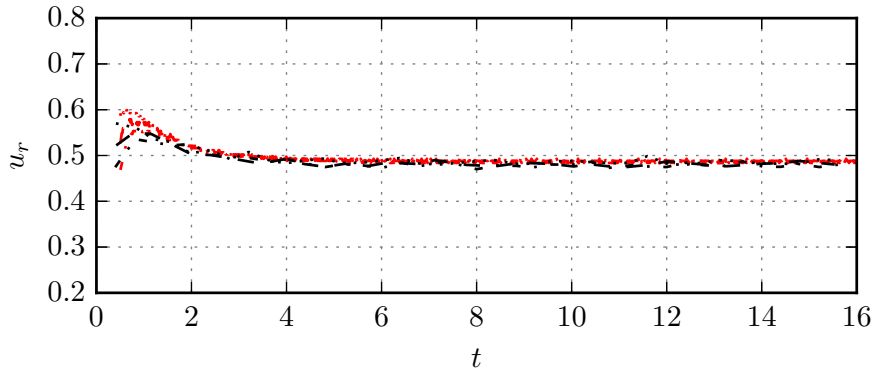

(a) Light front velocity

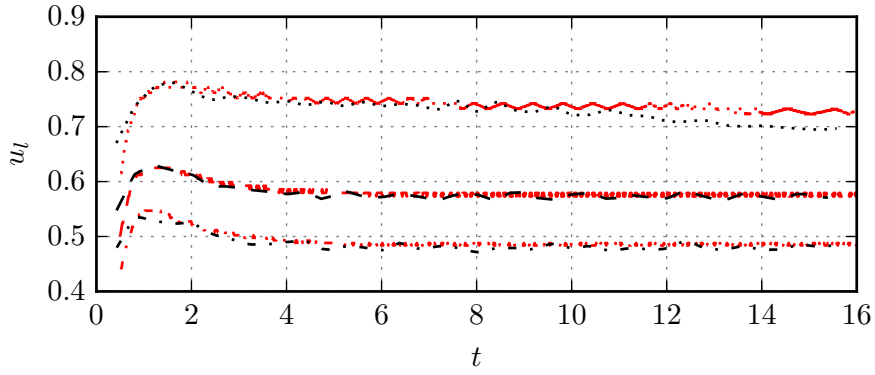

(b) Heavy front velocity

Figure 5: Comparison of the evolution of front velocities of the 2D lock exchange flow. Each figure shows the evolution of a front for density ratios: $\rho_2/\rho_1 = 0.998, 0.7, 0.4$ represented by dash-dotted, dashed and dotted lines respectively. The numerical results of Birman et al. [36] are presented in black whilst those of the present work are in red.

ever the present results show a maximum error in energy conservation of order $\mathcal{O}(0.1\%)$ whereas Birman et al. [36] report errors of order $\mathcal{O}(1\%)$; without this contribution the errors in energy conservation would be comparable.

4.2. Three-dimensional gravity currents

To further test QuasIncompact3D for application to gravity currents, 3D simulations are performed for the same density ratios as in §4.1, namely $\rho_2/\rho_1 = 0.998, 0.7, 0.4$. With the exception of the density ratios, the problem definition

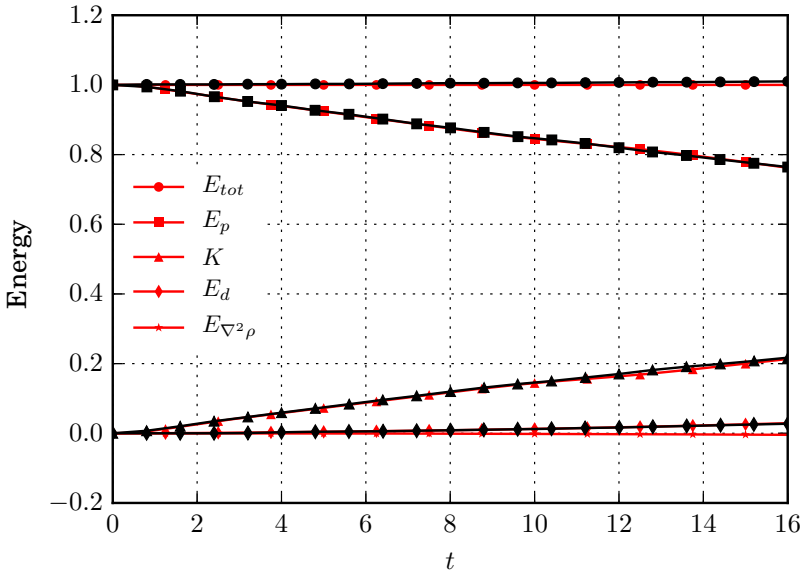

(a) Light front velocity

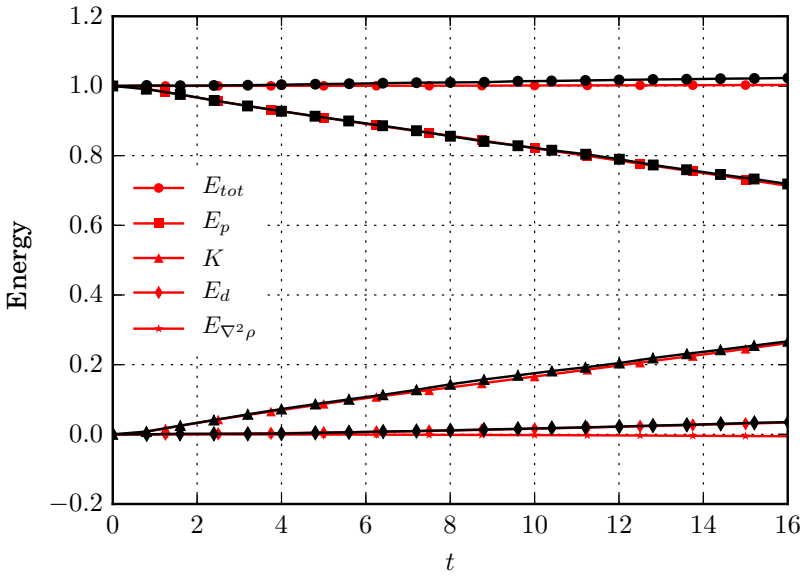

(b) Heavy front velocity

Figure 6: Comparison of the evolution of energy budgets of the 2D lock exchange flow for density ratios: $\rho_2/\rho_1 = 0.998, 0.4$. The figure legend indicates the different contributions to the overall energy budget. The numerical results of Birman et al. [36] are presented in black whilst those of the present work are in red.

is the same as for the non-sedimenting case of Espath et al. [37]: a 3D domain of dimensions $-H \leq x \leq 17H$, $0 \leq y, z \leq 2H$ containing an initially quiescent fluid of density ρ_1 in the subdomain $-H \leq x \leq 0$ and ρ_2 elsewhere with Reynolds number $Re = 2236$. Free-slip boundary conditions are applied in the x direction whilst on the y-normal boundaries a no-slip condition is applied for velocity and zero gradient for density; the problem is periodic in z. In this configuration the $\rho_2/\rho_1 = 0.998$ case approximately corresponds to the non-sedimenting Boussinesq simulation presented by Espath et al. [37].

To simulate the effect of removing a physical barrier between the subdomains at time $t = 0$, an initial perturbation is added to the velocity field according to

$$\boldsymbol{u}'(x) = |u'|\, e^{-\sigma\left(x - x_f^0\right)^2} \widehat{\boldsymbol{e}}\,, \tag{43}$$

where $\boldsymbol{u}'$ is the velocity perturbation, x_f^0 is the initial front location and $\widehat{\boldsymbol{e}}$ is the coordinate axis unit vector. The decay term is set to $\sigma = 25$ and the perturbations scaled such that the kinetic energy of the perturbed velocity field is 1% of the initially available potential energy, matching the approach taken by Espath et al. [9].

4.2.1. Mesh convergence

A mesh convergence study is performed for each case on meshes of $257 \times 33 \times 32$, $513 \times 65 \times 64$ and $1025 \times 129 \times 128$ mesh nodes, the highest resolution being approximately equivalent to that used by Espath et al. [9, 37]. To assess mesh convergence the location of the dense front and conservation of total energy are used as indicators. For brevity *fig.* 7 shows only the mesh convergence of $\rho_2/\rho_1 = 0.998$ as, being in the Boussinesq limit, it also allows comparison with the non-sedimenting results of Espath et al. [37].

As *fig.* 7a shows, there is good agreement with the Boussinesq simulation

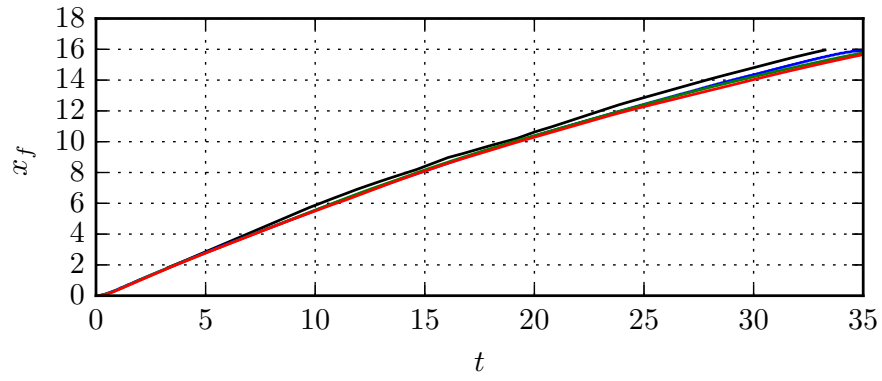

(a) Mesh convergence of front location.

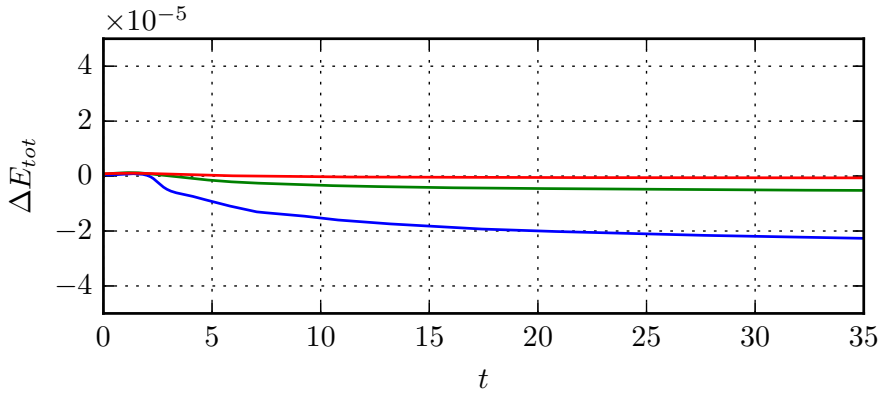

(b) Mesh convergence of energy conservation.

Figure 7: Mesh convergence study for 3D Boussinesq ($\rho_2/\rho_1 = 0.998$) case. The black line indicates the data from Espath et al. [37], data from the present work are for meshes: $257 \times 33 \times 32$ (blue); $513 \times 65 \times 64$ (green); and $1025 \times 129 \times 128$ (red).

performed by Espath et al. [37] and the present results for the front location and also that the front location is essentially mesh independent from the $513 \times 65 \times 64$ mesh to the $1025 \times 129 \times 128$ mesh. Using the conservation of total energy as a further indicator of mesh quality, *fig.* 7b shows that by using the finest mesh considered, the total energy is conserved to a high degree of accuracy with a peak error $\Delta E_{tot} \simeq \mathcal{O}\left(10^{-6}\right)$. The finest mesh is therefore judged to be good enough for fully resolved flows.

4.2.2. Effect of density ratio and 2D comparison

The 2D and 3D simulations are first compared using visualisations of the

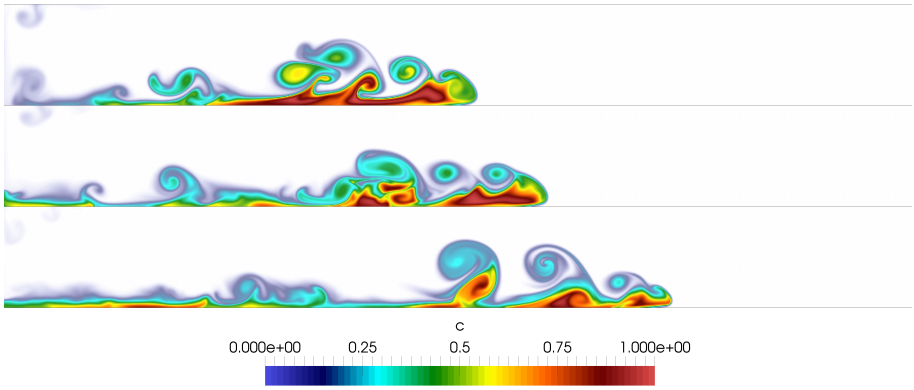

(a) Side view of 2D gravity currents.

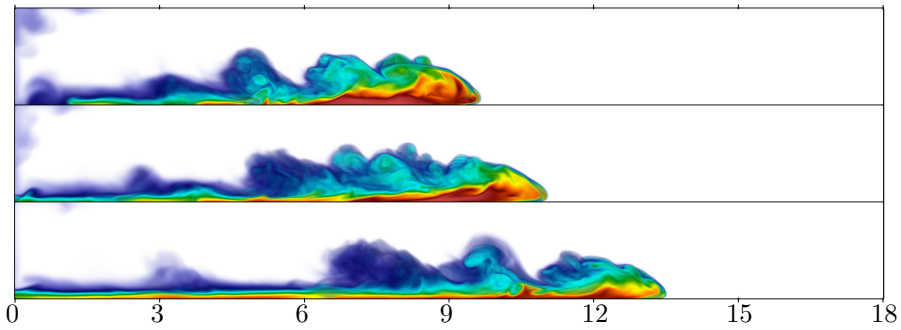

(b) Side view of 3D gravity currents.

Figure 8: Instantaneous visualisations of the 2D and 3D gravity currents at $t = 15$ showing the concentration field for density ratios $\rho_2/\rho_1 = 0.998, 0.7, 0.4$ from top-to-bottom.

concentration field for ρ_1 at time $t = 15$ in *fig.* 8. In each case a head region can be identified at the front of the gravity current which travels with increasing velocity as the density ratio increases. As detailed by Espath et al. [9] and references therein this development is driven by the fluid of the gravity current

"overstepping" the light fluid near the no-slip boundary at the bottom of the domain as visible in the curvature of the front. At the tail of the gravity current the heavier fluid is nearly settled at the bottom of the domain, the extent of this region increasing with density ratio as the current has travelled further. In between the head and tail is a region of significant vorticity which leads to significant mixing, in particular for the $\rho_2/\rho_1 = 0.4$ case where a large region of mixed fluids at the interface between the gravity current tail and head can be observed. Some important discrepancies between the 2D and 3D simulations concerning mainly the development of the Kelvin-Helmholtz instability and the resulting vorticity structures can be seen. In particular, very large scale coherent structures are present in the 2D simulations at the interface between the current and the ambient fluid. For the 3D simulations, lobe and cleft structures develop at the front of the current, as seen in *fig.* 9. These structures do not seem to be sensitive to the density ratio. A more detailed comparison between 2D

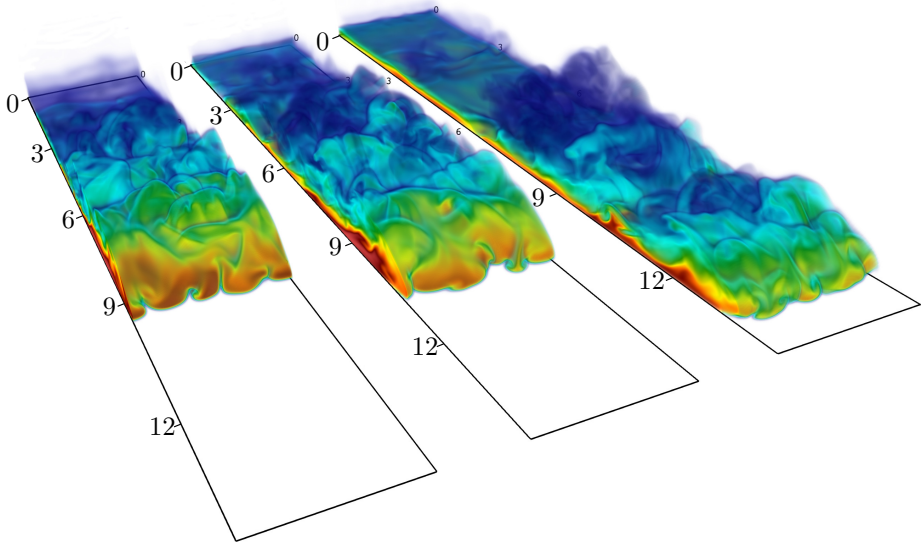

Figure 9: Perspective view of 3D gravity currents at $t = 15$ showing the concentration field for density ratios $\rho_2/\rho_1 = 0.998m0.7, 0.4$ from front-to-back. The colour scheme is the same as in *fig.* 8.

and 3D simulations can be achieved by looking at an arbitrary iso-contour (here $c = 0.9$, for clarity) of the concentration field (averaged in the spanwise direction for the 3D simulations) and at the temporal evolution of the front location. The data are presented in *fig.* 10 and *fig.* 11. The large coherent structures already reported in *fig.* 8 for the 2D simulations can also be seen in *fig.* 10. The concentration field seems to be more irregular for the 3D simulations with very little influence of the density ratio, except for the location of the front which is slightly further downstream of the initial lock when the density ratio is increased. As it can be seen in *fig.* 10, the 3D front always leads the 2D front, irrespective of the density ratio. This is true across all times up to the point when the fronts reach the end of the domain - after an initial period of almost matched velocity, the 2D front begins to decelerate whereas the 3D front maintains a near constant velocity until reaching the end of the domain. Figure 11 also shows that there is a dependency upon density ratio of this effect with the Boussinesq $\rho_2/\rho_1 = 0.998$ case showing the largest discrepancy between 2D and 3D front evolution and $\rho_2/\rho_1 = 0.4$ the smallest. It can be extrapolated that for very large density ratios, there would be no difference for the front location between 2D and 3D simulations.

5. Conclusion

A new variable-density Navier-Stokes solver has been implemented based on the open-source Incompact3D framework using the LMN approximation. The solver was validated for incompressible and LMN problems using the LMN approximation and its scalability demonstrated on several TIER-1/0 supercomputers. Although presented in the context of a solver for the LMN equations, in this work we demonstrate its general applicability to variable-density flows

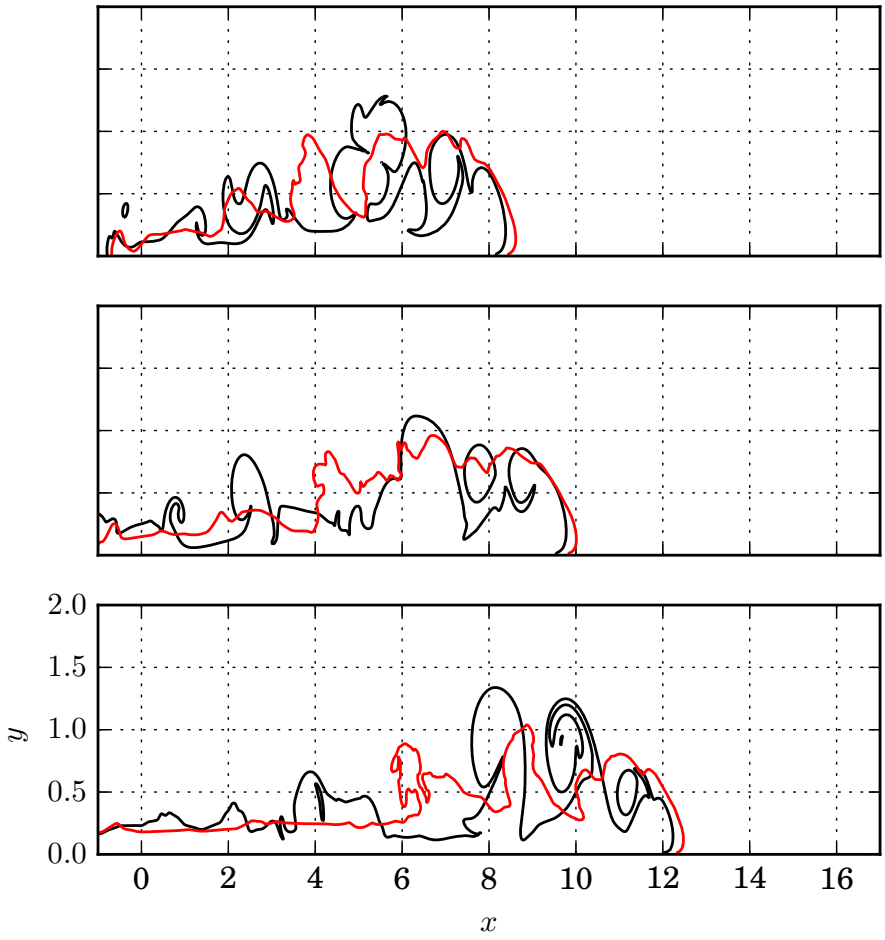

Figure 10: Comparison of 3D and 2D gravity currents by 3D (spanwise-averaged) and 2D $c = 0.9$ contours in red and black at $t = 15$ shown for density ratios $\rho_2/\rho_1 = 0.998, 0.7, 0.4$ from top-to-bottom.

in studying the gravity currents - this requires only appropriate modification to reflect changes to the continuity equation, the algorithm itself is unchanged.

The code was further validated for gravity currents in the lock-exchange configuration over a range of density ratios and the finite release configuration in the Boussinesq limit, demonstrating a good agreement with data from two different studies and in two- and three-dimensions. In comparing with the 2D

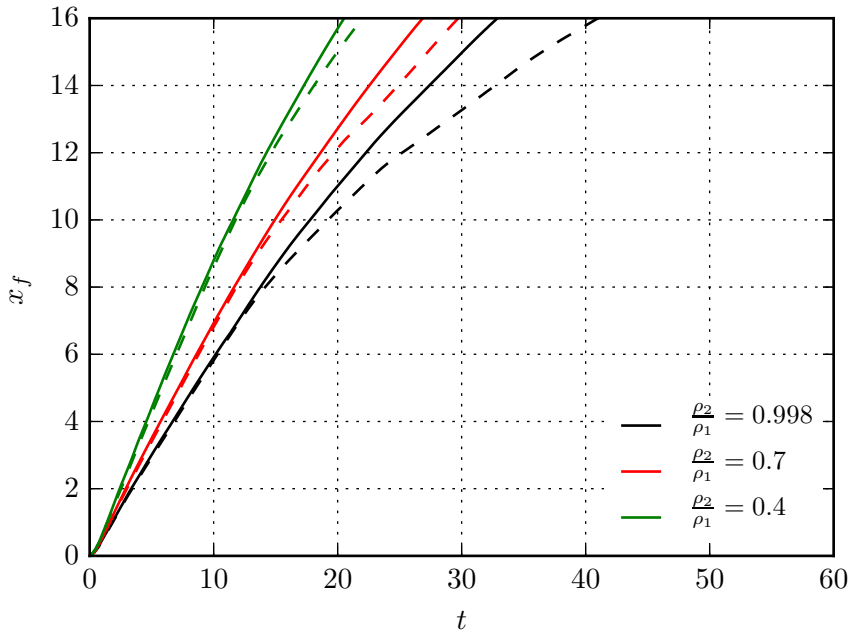

Figure 11: The evolution of the front location over time for 3D (solid line) and 2D (dashed line) simulations for density ratios $\rho_2/\rho_1 = 0.998, 0.7, 0.4$ (black, red, green respectively).

results of Birman et al. [36] the necessity to properly account for all contributions of the energy budget was demonstrated. By doing so, the present results are in good agreement with the reference data, but by including all sources of energy dissipation the error in energy conservation is reduced, allowing greater confidence in the present results.

For high-resolution simulations of 2D and 3D finite release gravity currents it was observed that after an initial period differences develop. For times ($t \gtrsim 10$) the location of the dense front in the 3D simulations is ahead of the 2D one as the front slows down more severely in the 2D results. A visual examination of the instantaneous concentration contours shown in *fig.* 10 shows that the 2D contours have a greater undulation than the 3D ones. This undulation would indicate energy expenditure in the vertical direction and may explain the slowing

of the front for the 2D flow simulations. An additional observation is that this difference of behaviour appears to be inversely related to the density ratio with the simulations performed within the Boussinesq limit in this work showing the largest discrepancy between 2D and 3D results. These results may explain the contrasting results of Bonometti et al. [16], Espath et al. [9], Étienne et al. [15], Necker et al. [8], Rotunno et al. [17]. Based on these preliminary results, further studies of non-Boussinesq gravity currents are required to determine the physical mechanisms causing the differences between the 2D and 3D results and investigate the reason for the observed difference being greater in the Boussinesq limit. A further aspect of this future work is to investigate the effect of the Reynolds and Schmidt numbers on non-Boussinesq gravity currents.

6. Acknowledgements

The authors would like to thank EPCC for funding this work through [grant number eCSE10-02]. Computing time was provided on `ARCHER` by the EPCC [grant number eCSE10-02] and the UK turbulence consortium [grant number EP/R029321/1] and on `MARCONI` and `HAZEL HEN` by PRACE [grant numbers 2016 163847 and 2018 184381]. Additional computing time was provided by the Imperial College Research Computing Service [38]. The authors would also like to thank Eric Lamballais whose insightful comments on the manuscript are much appreciated.

7. Computer code availability

The code used in this work is available at: https://github.com/xcompact3d/Quasincompact3d.

[1] S. Laizet, E. Lamballais, High-Order Compact Schemes for Incompress-

ible Flows: A Simple and Efficient Method with Quasi-Spectral Accuracy, Journal of Computational Physics 228 (16) (2009) 5989–6015.

[2] S. K. Lele, Compact Finite Difference Schemes with Spectral-like Resolution, Journal of Computational Physics 103 (1) (1992) 16–42.

[3] S. Laizet, N. Li, Incompact3d: A Powerful Tool to Tackle Turbulence Problems with up to O(10^5) Computational Cores, International Journal for Numerical Methods in Fluids 67 (11) (2011) 1735–1757.

[4] H. E. Huppert, Geological Fluid Mechanics, Perspectives in fluid dynamics: A collective introduction to current research (2000) 447–506.

[5] K. L. Seitter, A Numerical Study of Atmospheric Density Current Motion Including the Effects of Condensation, Journal of the Atmospheric Sciences 43 (24) (1986) 3068–3076.

[6] G. W. Lennon, D. G. Bowers, R. A. Nunes, B. D. Scott, M. Ali, J. Boyle, C. Wenju, M. Herzfeld, G. Johansson, S. Nield, P. Petrusevics, P. Stephenson, A. A. Suskin, S. E. A. Wijffels, Gravity Currents and the Release of Salt from an Inverse Estuary, Nature 327 (6124) (1987) 695.

[7] C. Härtel, E. Meiburg, F. Necker, Analysis and Direct Numerical Simulation of the Flow at a Gravity-Current Head. Part 1. Flow Topology and Front Speed for Slip and No-Slip Boundaries, Journal of Fluid Mechanics 418 (2000) 189–212.

[8] F. Necker, C. Härtel, L. Kleiser, E. Meiburg, High-Resolution Simulations of Particle-Driven Gravity Currents, International Journal of Multiphase Flow 28 (2) (2002) 279–300.

[9] L. Espath, L. Pinto, S. Laizet, J. Silvestrini, Two- and Three-Dimensional

Direct Numerical Simulation of Particle-Laden Gravity Currents, Computers & Geosciences 63 (2014) 9–16.

[10] A. Dai, High-Resolution Simulations of Downslope Gravity Currents in the Acceleration Phase, Physics of Fluids 27 (7) (2015) 076602.

[11] A. Dai, C.-S. Wu, High-Resolution Simulations of Cylindrical Gravity Currents in a Rotating System, Journal of Fluid Mechanics 806 (2016) 71–101.

[12] R. Inghilesi, C. Adduce, V. Lombardi, F. Roman, V. Armenio, Axisymmetric Three-Dimensional Gravity Currents Generated by Lock Exchange, Journal of Fluid Mechanics 851 (2018) 507–544.

[13] L. Ottolenghi, C. Adduce, F. Roman, V. Armenio, Analysis of the Flow in Gravity Currents Propagating up a Slope, Ocean Modelling 115 (2017) 1–13.

[14] L. Ottolenghi, P. Prestininzi, A. Montessori, C. Adduce, M. La Rocca, Lattice Boltzmann Simulations of Gravity Currents, European Journal of Mechanics - B/Fluids 67 (2018) 125–136.

[15] J. Étienne, E. J. Hopfinger, P. Saramito, Numerical Simulations of High Density Ratio Lock-Exchange Flows, Physics of Fluids 17 (3) (2005) 036601.

[16] T. Bonometti, S. Balachandar, J. Magnaudet, Wall Effects in Non-Boussinesq Density Currents, Journal of Fluid Mechanics 616 (2008) 445–475.

[17] R. Rotunno, J. B. Klemp, G. H. Bryan, D. J. Muraki, Models of Non-Boussinesq Lock-Exchange Flow, Journal of Fluid Mechanics 675 (2011) 1–26.

[18] T. Bonometti, M. Ungarish, S. Balachandar, A Numerical Investigation of High-Reynolds-Number Constant-Volume Non-Boussinesq Density Currents in Deep Ambient, Journal of Fluid Mechanics 673 (2011) 574–602.

[19] A. Dai, Y.-l. Huang, High-resolution simulations of non-Boussinesq downslope gravity currents in the acceleration phase, Physics of Fluids 28 (2) (2016) 026602.

[20] P. A. McMurtry, W.-H. Jou, J. Riley, R. W. Metcalfe, Direct Numerical Simulations of a Reacting Mixing Layer with Chemical Heat Release, AIAA Journal 24 (6) (1986) 962–970.

[21] S. P. Jammy, C. T. Jacobs, N. D. Sandham, Performance Evaluation of Explicit Finite Difference Algorithms with Varying Amounts of Computational and Memory Intensity, Journal of Computational Science (in press).

[22] Z. J. Wang, K. Fidkowski, R. Abgrall, F. Bassi, D. Caraeni, A. Cary, H. Deconinck, R. Hartmann, K. Hillewaert, H. T. Huynh, N. Kroll, G. May, P.-O. Persson, B. van Leer, M. Visbal, High-Order CFD Methods: Current Status and Perspective, International Journal for Numerical Methods in Fluids 72 (8) (2013) 811–845.

[23] F. Golanski, V. Fortuné, E. Lamballais, Noise Radiated by a Non-Isothermal, Temporal Mixing Layer. Part II: Prediction Using DNS in the Framework of Low Mach Number Approximation, Theoretical and Computational Fluid Dynamics 19 (6) (2005) 391–416.

[24] E. Motheau, J. Abraham, A High-Order Numerical Algorithm for DNS of Low-Mach-Number Reactive Flows with Detailed Chemistry and Quasi-Spectral Accuracy, Journal of Computational Physics 313 (2016) 430–454.

[25] A. W. Cook, J. J. Riley, Direct Numerical Simulation of a Turbulent Reactive Plume on a Parallel Computer, Journal of Computational Physics 129 (2) (1996) 263–283.

[26] A. J. Chorin, A Numerical Method for Solving Incompressible Viscous Flow Problems, Journal of Computational Physics 135 (2) (1997) 118–125.

[27] F. Nicoud, Numerical Study of a Channel Flow with Variable Properties. CTR Annual Research Briefs 1998, Tech. Rep., Stanford University/NASA Ames, 1999.

[28] F. Nicoud, Conservative High-Order Finite-Difference Schemes for Low-Mach Number Flows, Journal of Computational Physics 158 (1) (2000) 71–97.

[29] EPCC, ARCHER, https://www.archer.ac.uk/, 2018.

[30] CINECA, MARCONI, https://www.cineca.it/en/content/marconi, 2018.

[31] HLRS, Hazel Hen, https://www.hlrs.de/systems/cray-xc40-hazel-hen/, 2018.

[32] J. Kim, W. J. Dally, S. Scott, D. Abts, Technology-driven, highly-scalable dragonfly topology, in: Computer Architecture, 2008. ISCA'08. 35th International Symposium on, IEEE, 77–88, 2008.

[33] M. E. Brachet, D. I. Meiron, S. A. Orszag, B. G. Nickel, R. H. Morf, U. Frisch, Small-Scale Structure of the Taylor–Green Vortex, Journal of Fluid Mechanics 130 (1983) 411–452.

[34] T. Dairay, E. Lamballais, S. Laizet, J. C. Vassilicos, Numerical Dissipation vs. Subgrid-Scale Modelling for Large Eddy Simulation, Journal of Computational Physics 337 (2017) 252–274.

[35] V. Fortuné, E. Lamballais, Y. Gervais, Noise Radiated by a Non-Isothermal, Temporal Mixing Layer. Part I: Direct Computation and Prediction Using Compressible DNS, Theoretical and Computational Fluid Dynamics 18 (1) (2004) 61–81.

[36] V. K. Birman, J. E. Martin, E. Meiburg, The Non-Boussinesq Lock-Exchange Problem. Part 2. High-Resolution Simulations, Journal of Fluid Mechanics 537 (2005) 125–144.

[37] L. F. R. Espath, L. C. Pinto, S. Laizet, J. H. Silvestrini, High-Fidelity Simulations of the Lobe-and-Cleft Structures and the Deposition Map in Particle-Driven Gravity Currents, Physics of Fluids 27 (5) (2015) 056604.

[38] ICRS, Imperial College Research Computing Service, https://www.imperial.ac.uk/admin-services/ict/self-service/research-support/rcs/impact/citing-the-service/, 2018.